

Heterogeneous Gas-Phase Synthesis and Molecular Dynamics Modeling of Janus and Core–Satellite Si–Ag Nanoparticles

Vidyadhar Singh,[†] Cathal Cassidy,^{*,†} Panagiotis Grammatikopoulos,[†] Flyura Djurabekova,[‡] Kai Nordlund,[‡] and Mukhles Sowwan^{*,†,§}

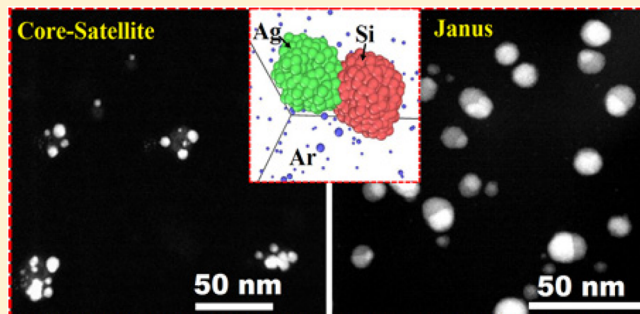
[†]Nanoparticles by Design Unit, Okinawa Institute of Science and Technology (OIST) Graduate University, 1919-1 Onna-Son, Okinawa 904-0495, Japan

[‡]Department of Physics and Helsinki Institute of Physics, University of Helsinki, P.O. Box 43, FIN-00014 Helsinki, Finland

[§]Nanotechnology Research Laboratory, Al-Quds University, P.O. Box 51000, East Jerusalem, Palestine

Supporting Information

ABSTRACT: Heterogeneous gas-phase condensation is a promising method of producing hybrid multifunctional nanoparticles with tailored composition and microstructure but also intrinsically introduces greater complexity to the nucleation process and growth kinetics. Herein, we report on the synthesis and growth modeling of silicon–silver (Si–Ag) hybrid nanoparticles using gas-aggregated cosputtering from elemental Si and Ag source targets. The final Si–Ag ensemble size was manipulated in the range 5–15 nm by appropriate tuning of the deposition parameters, while variations in the Si–Ag sputtering power ratio, from 1.8 to 2.25, allowed distinctive Janus and core–satellite structures, respectively, to be produced. Molecular dynamics simulations indicate that the individual species first form independent clusters of Si and Ag without significant intermixing. Collisions between unlike species are unstable in the early stages of growth (<100 ns), with large temperature differences resulting in rapid energy exchange and separation. Upon further cooling and depletion of isolated Si and Ag atoms through collection by parent clusters (>100 ns), Si–Ag cluster collisions ultimately result in stable hybrid structures.



INTRODUCTION

Hybrid multifunctional nanoparticles are attractive for a variety of applications (such as catalysis, optoelectronic devices, and biomedicine) and may possess enhanced chemical and physical properties resulting from the interaction of the different constituent materials.^{1–6} Such heterostructured nanoparticles have typically been prepared by seed-mediated reactions in which stable single crystalline or amorphous core particles are used to seed the formation of the shell component using wet chemical methods or chemical vapor deposition processes.^{7–11} However, in these approaches, controlled growth is challenging, and residual contamination both at the interface between the different components and on the surface compromises the properties.^{9–11}

Physical vapor deposition (PVD, or sputtering) is a ubiquitous deposition technique, offering relatively fast, good quality, and cost-efficient depositions.^{12–21} PVD synthesized nanostructures are advantageous for technological applications that require controlled and contamination-free synthesis, such as the fabrication of nanoelectronic devices.¹² For nanoparticle synthesis, since the pioneering work of Haberland et al.,¹⁵ rapid advances in magnetron-sputter gas-phase condensation of single component metal and semiconductor nanoparticles have been made.^{16–18} Control over deposition parameters

like magnetron power, aggregation zone length, and inert gas pressure, in combination with *in situ* mass filtration, has allowed for the growth of size-selected nanoparticles with great accuracy.^{16–19}

Further progress in gas-phase synthesis was made by sputtering alloys to expand the nanoparticle composition from single-component to hybrid multicomponent heterostructures.^{20,21} For example, Xu et al.²⁰ reported experimental work on iron–silver (Fe–Ag) heterostructured nanoparticles with a dumbbell-like shape, and Yin et al.²¹ described fabrication of magnetic-plasmonic, cobalt–gold (Co–Au) nanoparticles with a core–shell structure, originating from a single-alloy sputtering target. However, utilizing single-alloy targets suffers from some disadvantages, such as reduced versatility in compositional ratios or unworkable single target preparation owing to bulk immiscibility in the solid state.

The Si–Ag system exemplifies the limitations of single alloy targets, given that these materials are immiscible in the bulk solid state.^{22,23} Si–Ag nanoparticles are, however, of significant interest because the combined semiconductor/metal system

Received: January 20, 2014

Revised: June 1, 2014

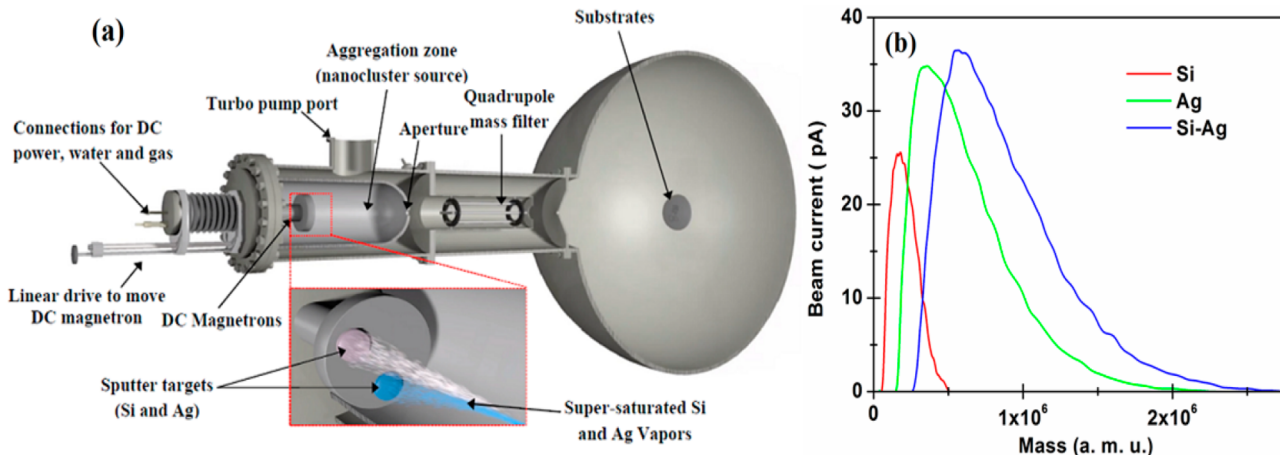


Figure 1. (a) Illustration of the magnetron sputter inert gas condensation set up used for the deposition of hybrid Si–Ag nanoparticles and (b) quadrupole mass filter (QMF) profile showing the mass distribution of individual Si, Ag, and Si–Ag nanoparticles.

exhibits both photoluminescence and plasmonic properties.^{24–26} Previous attempts have been limited to chemical methods; for example, Chen et al.^{24,25} reported a modified Stöber method for the synthesis of $\text{SiO}_2@\text{Ag}$ core–satellite nanoparticles, which can be used for plasmonic-based chemical sensing and photocatalysis applications. Ferry and co-workers designed Si–Ag plasmonic nanostructures for ultrathin solar cells that exhibit enhanced absorption.²⁶

In contrast to previous wet synthesis methods, herein we report on Si–Ag nanoparticles fabricated via gas-aggregated cosputtering of Si and Ag from two independent neighboring targets. The growth conditions and resultant microstructure were investigated by atomic force microscopy (AFM), aberration-corrected scanning transmission electron microscopy (STEM) in high angle annular dark field (HAADF) mode, and high resolution transmission electron microscopy (HRTEM) in bright field mode. Molecular dynamics (MD) computer simulations were utilized to gain an insight into the growth process and to explain the resultant hybrid nanoparticle structures and crystallinity.

EXPERIMENTAL SECTION

Materials. The Si magnetron-sputtering target (Si n-type, purity >99.99%, resistivity <0.001 $\Omega\cdot\text{m}$) and Ag magnetron sputtering target (Ag, purity >99.99%, resistivity $\sim 2 \times 10^{-8} \Omega\cdot\text{m}$) with dimensions of 25 mm diameter \times 3 mm thickness were purchased from Kurt J. Lesker (Pittsburgh, PA). As substrates for AFM measurements, undoped Si dice with (100) orientation and 5 mm \times 5 mm in size were purchased from MTI Corporation (Richmond, CA). Cu frames (400 mesh) with electron transparent carbon membranes were purchased from Ted Pella Inc. (Redding, CA) as substrates for TEM/STEM-HAADF analysis.

Hybrid Nanoparticles Synthesis. The Si–Ag nanoparticles were synthesized from the gas-phase using magnetron sputtering, as illustrated in Figure 1a. The deposition system consists of a nanocluster sputtering source, a quadrupole mass filter (QMF), and a deposition chamber. Si and Ag sputtering targets were located side by side on an integrated magnetron sputtering head, as shown in Figure 1a (inset). The size of the nanoparticles, as well as the volume fraction of each component, was controlled by tuning the magnetron power applied on each target independently while cosputtering.

Preliminary studies were conducted to identify a suitable deposition parameter window for both materials, via *in situ* QMF feedback and deposited cluster characterization. Corresponding *in situ* mass spectra, showing a comparison of mass variations of selected Si, Ag, and Si–Ag nanoparticle beams, are presented in Figure 1b. This *in-flight* measurement gives invaluable “live” feedback on the cluster formation process. Subsequently, for all reported depositions, the Ar and He flow rates were set to 70 and 5 sccm, respectively, resulting in an aggregation zone pressure reading of 2.5×10^{-1} mbar. The aggregation zone length was set to 125 mm. The base pressure was 7.0×10^{-8} mbar in the main deposition chamber. With the Si target sputtering power held fixed at 90 W, the tuning of the particle composition, size, and shapes was achieved by varying the sputtering power supplied to the Ag target, from a minimum of 30 W to a maximum of 60 W. For AFM and TEM/STEM measurements, monodispersed nanoparticles were directly deposited on diced silicon substrates and TEM grids, at room temperature. The surface coverage was controlled by deposition time. Substrate table rotation was set at 2 rpm for all depositions to ensure uniform coverage.

Characterization. AFM measurements were performed in a glovebox environment (<0.1 ppm O₂ and <1 ppm water) using a Multimode 8 (Bruker, Santa Barbara, CA) AFM system equipped with the NanoScope-V controller in tapping mode using triangular silicon-nitride AFM tip (radius <5 nm, force constant of 0.35 N m⁻¹, 65 kHz of resonant frequency, Bruker). The scanning probe processor (SPIP) (Image Metrology, Hørsholm, DK) software was used for the analysis of the images. TEM grids loaded with Si–Ag nanoparticles were exposed to atmosphere before loading into the microscope (resulting in oxidation). TEM studies were carried out using a 300 kV FEI Titan microscope, equipped with a spherical aberration corrector for the probe (for STEM imaging). In TEM mode the spherical and chromatic aberrations were 1.2 and 1.6 mm, respectively. Point resolution was ~ 0.20 nm, at Scherzer defocus conditions of -50 nm to +60 nm. In STEM mode, the spherical aberration was in the range 0–5 μm , with chromatic aberration of 1.8–2.0 mm. Optimum HAADF–STEM resolution was approximately 0.1 nm. Energy dispersive X-ray spectroscopy (EDX) was performed with an Oxford X-max system, with an 80 mm² silicon drift detector (SDD) and energy resolution of 136 eV.

Molecular Dynamics Simulation Method. We applied MD computer simulations²⁷ to gain further understanding of the growth behavior and interactions of the nascent nanoclusters. Our model was designed to correspond to the conditions in the aggregation zone in the experimental setup (Figure 1a) and was based on methods employed in the past to simulate simpler, single-element, systems.^{28–32} In a cubic box with a side length of 40 nm and periodic boundary conditions, Si, Ag, and Ar atoms were introduced at random positions, but ensuring they were initially isolated from each other. Several combinations of atomic concentrations were examined, with the number of atoms of each element ranging between 50 and 1000. This way, various experimental parameters were approximated, with changes in the numbers of atoms of the two sputtered species corresponding to variations in discharge powers and changes in the number of Ar atoms corresponding to variations in inert gas pressure.

Atomic Si–Si and Ag–Ag interactions were modeled with the well-established Stillinger–Weber and Foiles embedded atom method (EAM) interatomic potentials, respectively,^{33–35} whereas the Si–Ag interatomic interaction was modeled with a pair potential based on a dimer potential calculated with a density-functional theory approach,³⁶ rescaled to predict Si–Ag mixing in the liquid phase but segregating in the solid phase,³³ in accordance with the Si–Ag phase diagram.³⁷ Interactions between Ar and Si/Ag atoms were represented by universal, purely repulsive potentials developed by Ziegler, Biersack, and Littmark (ZBL),³⁸ whereas the Lennard-Jones potential was utilized to represent forces between Ar atoms.³⁹ The initial velocities of the monomers in our model corresponded to a temperature of 6000 K. No radiative cooling was employed; instead, Ar gas atoms acted as a cooling agent to correspond to the experimental situation of cluster condensation occurring in a flow of a larger volume of Ar inert gas. The Berendsen thermostat⁴⁰ set to room temperature was applied to Ar atoms alone, every time they passed through any of the boundaries. In this way, the Ar atoms were able to facilitate the cooling down of the Si/Ag system, carrying away the excess energy they acquired upon collisions with the initially hot Si/Ag atoms. The total simulation times were $\sim 0.2 \mu\text{s}$.

RESULTS AND DISCUSSION

In Situ Size and Morphology Control. The nanocluster mass distribution dependence on the synthesis parameters was determined *in situ* by the QMF spectrometer, capable of high-resolution measurement and filtering of nanoparticles between 1×10^3 and 3×10^6 amu, prior to the actual depositions. For example, a comparison of mass variations of selected Si, Ag, and Si–Ag nanoparticle beams is presented in Figure 1b. The integrated nanocluster beam currents obtained from individual cluster beams of Si and Ag when added together closely match the integrated nanocluster current obtained from the hybrid Si–Ag cluster beam. After substrate landing and load-lock transfer, the nanoparticle coverage and size distribution were measured via AFM. Figure 2 shows typical AFM topography images and size distributions of Si–Ag hybrid nanoparticles deposited with 30, 40, 50, and 60 W Ag target magnetron power, respectively, while the magnetron power on the Si target was kept constant at 90 W. We obtained a height distribution for each of the four deposition cases, as shown in Figure 2. Here, we were able to produce Si–Ag nanoparticles with four different sizes: 4.5 ± 2.0 , 6.5 ± 3 , 10 ± 4 , and 15 ± 8 nm, which

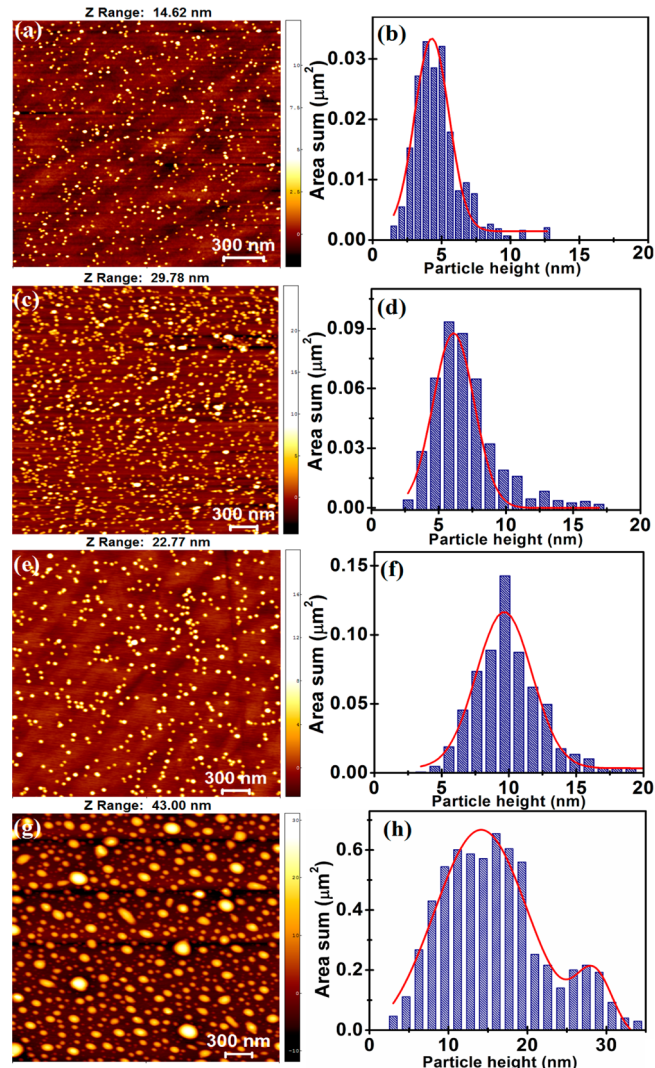


Figure 2. AFM topography images and height distributions with fitted Gaussian curves for Si–Ag multicomponent nanoparticles, (a, b) 4.5 nm (c, d) 6.5 nm, (e, f) 10 nm, and (g, h) 15 nm, produced using a variety of different deposition conditions. The possibility to directly control the overall nanoparticle size distribution using this deposition technology is clearly demonstrated by these AFM scans. Note that the larger peak of the double distribution seen in (h) is caused by particles which exceed the size limit of the QMF.

highlights directly the controlled variation in particle sizes that can be achieved with this deposition configuration.

While AFM scans provide basic information about size distribution, high resolution electron microscopy allows us to determine the microstructure, crystallinity, and elemental distribution of Si and Ag within the hybrid ensembles. Representative images are shown in Figure 3. Bright field TEM (Figure 3a,b) and HAADF STEM micrographs (Figure 3c,d) reveal two types of structures, namely core–satellite and Janus Si–Ag hybrid nanoparticles. Janus particles refer to those having a roughly spherical external morphology but composed of roughly hemispherical volumes of each constituent element.³ Core–satellite particles refer to those having a larger core nanoparticle, on the surface of which a number of smaller clusters, of the other element, reside.²⁵ We assume that the surface of the Si nanoparticles was oxidized after exposure to air (while transporting to the TEM), as seen previously.³³ When

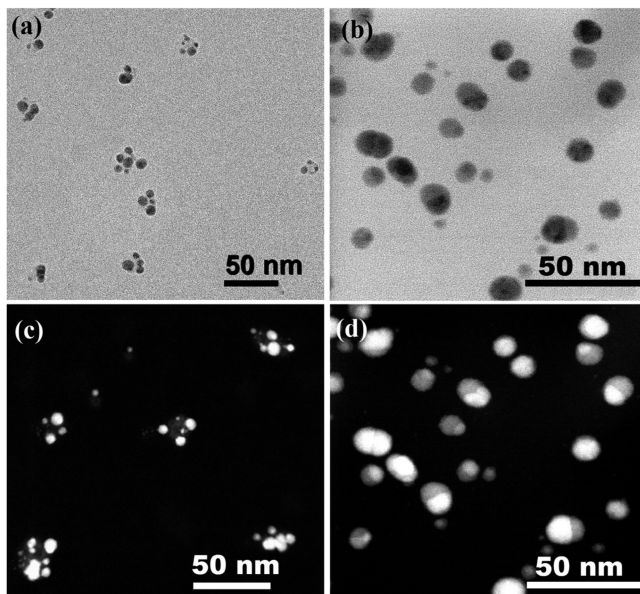


Figure 3. Transmission electron micrographs of hybrid Si–Ag nanoparticles (a, b), bright-field HRTEM and (c, d) HAADF-STEM images of the (a, c) core–satellite, and (b, d) Janus Si–Ag nanoparticles. The Si/Ag sputtering power ratios were 2.25 and 1.8, respectively. In bright field TEM (a, b), the crystalline Ag domains appear dark, resulting from diffraction of the electron beam by the ordered lattice. In the HAADF-STEM micrographs (c, d), the higher-Z Ag regions appear bright because the higher atomic number of Ag results in a stronger detected signal (i.e., more scattered electrons striking the high-angle off-axis detector), relative to Si. The different microstructures resulting from the different Si/Ag sputtering power ratios can clearly be observed.

lower magnetron powers were applied to the Ag sputtering target, hybrid nanoparticles with Si cores decorated with several Ag nanoclusters (Figure 3a,c) were observed (the core–satellite structure). At higher Ag magnetron powers, hybrid nanoparticles with more symmetrical Si–Ag regions were observed (Figure 3b,d). In this case, most of the particles have Janus structures,³ composed of distinct equi-sized Ag and Si regions. The elemental makeup was confirmed by EDX analysis (see Figure S1 in the Supporting Information). No Ag X-ray counts were detected from the neighboring Si regions (see Figure S1b), and vice versa. Note that formation of such structures is also possible after deposition, via coalescence on the substrate,¹⁹ but this has been ruled out in our case (see Figure S5 and associated explanatory caption). As a result, we assume that these structures formed exclusively in-flight from target to substrate.

Figure 4 shows high-resolution TEM and HAADF-STEM images of hybrid clusters. High resolution imaging revealed that Ag domains are consistently crystalline while Si domains are consistently amorphous (Figure 3c,d), both for the core–satellite and the Janus structure. Corresponding indexed FFT patterns are presented in Figure S2. The images and associated FFTs are consistent with face-centered cubic (FCC) Ag structure with a lattice parameter of 0.4086 nm: (111) [$d_{111} = 0.2352 \text{ nm}$], (200) [$d_{200} = 0.2001 \text{ nm}$], and (220) [$d_{220} = 0.1443 \text{ nm}$]. The disordered and crystalline structures of Si and Ag, respectively, are in agreement with the previously reported results for both of these materials, when sputtered separately but under otherwise comparable conditions (see Figures S3 and S4).⁴¹ Additionally, this observation provides an interesting

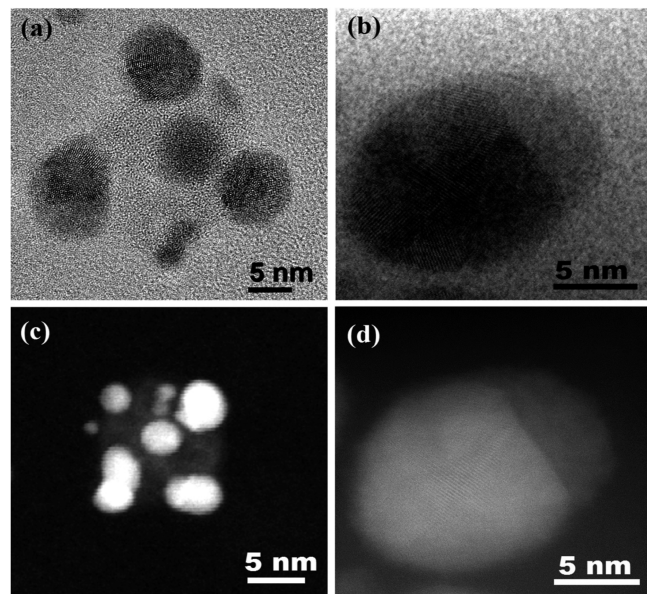


Figure 4. Bright-field HRTEM (a, b) and HAADF-STEM (c, d) image of the core–satellite (a, c) and Janus (b, d) Si–Ag nanoparticles, respectively. These images indicate that Si and Ag elements are localized into well-defined regions. From the examination of many HRTEM images of Ag nanoparticle Si interface, we found that most Ag nanoparticles are single crystalline while a few reveal twinning boundary defects.

counterpoint to recent work by the authors,³³ in which conventional sputtering of Ag atoms onto preformed Si clusters, in-flight, was found to crystallize the Si in a controlled fashion. Clearly, a different mechanism is at play for this changed synthesis configuration and is discussed in the following modeling section.

Hybrid Nanocluster Growth Modeling. The growth kinetics and observed microstructures can be understood via comparison with MD simulations. A number of different configurations containing various percentages of the two sputtered materials were investigated, for various carrier gas concentrations, all yielding comparable results. For a clear, coherent demonstration of the synthesis process, the simulation run containing 500 atoms of each species is chosen as an example case, since it features all the significant events of the aggregation mechanism in just one sequence of events. A full-length animation of this simulation is included in the Supporting Information (Movie S1). Starting with a supersaturated vapor of Si and Ag atoms (Figure 5a), the first observation has been that the two species, Si and Ag, initially clustered independently. No mixed-species dimers, trimers, or small primary particles were formed. Both species nucleated and grew individually. The dominating mechanism for nucleation was via three-body collisions,^{30,42–45} with Ar atoms carrying away the excess energy (Figure 5b). Subsequent growth was smooth and gradual, with individual atoms landing on already formed cluster seeds (Figure 5c). Eventually, the simulation box became depleted of monomers, and more violent events happened, as growth was mainly governed by cluster aggregation. It was at this last stage only that mixed clustering could occur (Figure 5d,e), as is expanded in detail in the following discussion elucidating the thermal evolution of the system.

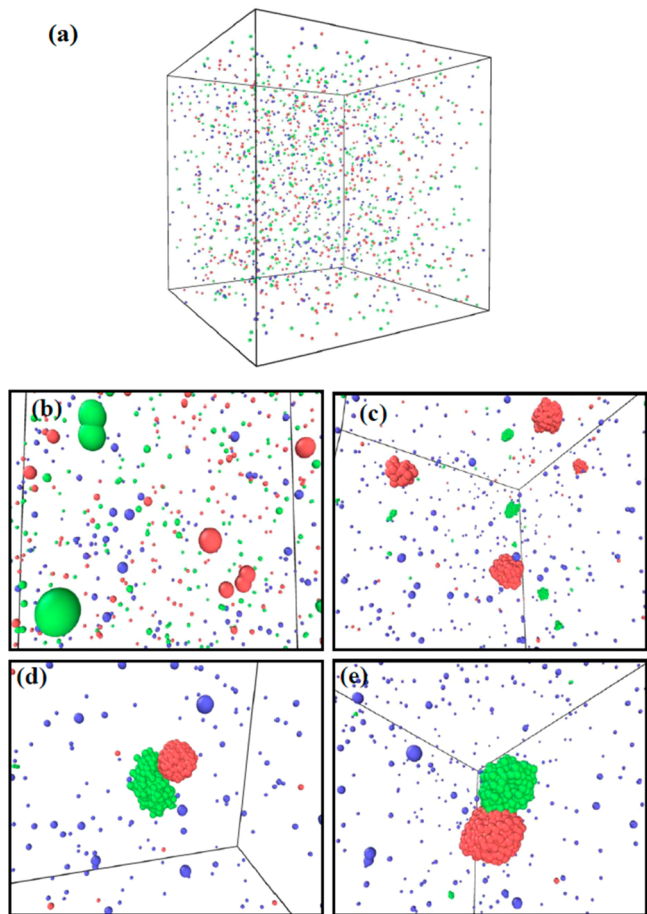


Figure 5. MD computer simulation of simultaneous cosputtering and growth of Si–Ag nanoparticles. (a) Initial configuration (0 ns), containing 500 Si, 500 Ag, and 500 Ar atoms (red, green, and blue spheres, respectively) at random initial positions. (b) Aggregation begins by formation of dimers of both species (~5 ns). (c) Primary particles are formed separately (~30–75 ns). (d) Unstable Janus cluster forms by partial coalescence of particles of different species (~78 ns). Note that these clusters separate again after approximately 4 ns, as can be seen in the animation file in the Supporting Information. (e) Upon subsequent collisions, the particles are cooled sufficiently to form a stable Janus structure (~110 ns). Simulation results visualized using Ovito.⁴⁷

The temperature of the nascent clusters is a key parameter which governs their coalescence and interaction. Figure 6 shows the time development of the partial temperatures (in K), in a system containing 500 atoms of each species. Note that the regions I–V in Figure 6 correspond directly to the snapshots shown in Figure 5a–e, respectively. At first, both sputtered species are cooled simultaneously via collisions with Ar gas (region I, Figure 6). In principle, the cooling rates rely on the mass difference between inert gas and vapor atoms,^{28,46} which means that Ag should lose heat faster. Nevertheless, the big number of Ar atoms and the resulting big number of collision events make this difference insignificant, and both species cool down almost at the same rate. Once the partial temperatures have been sufficiently lowered, dimers start forming (region II, Figure 6). The dimer heat of formation is (in accord with the equipartition theorem) transformed into kinetic energy, i.e., heating the nascent cluster nuclei. As a result, the temperature subsequently starts to increase, which explains the minimum in the temperature curves at about 5 ns. It is noteworthy that, after

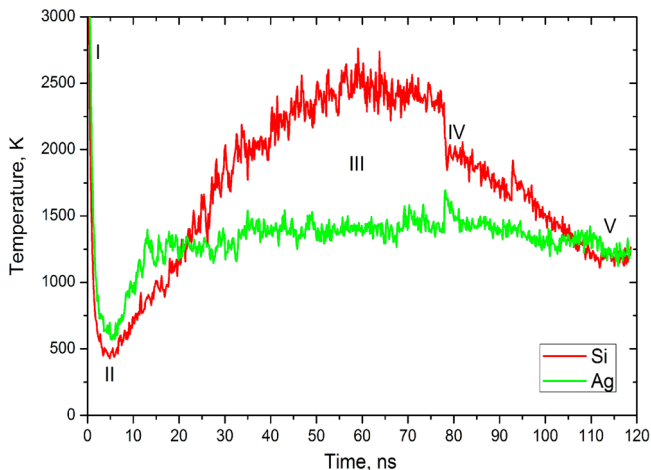


Figure 6. Time development of temperature (in K). Regions I–V correspond to Figure 5a–e and designate initial configuration, formation of dimers, aggregation in primary, single-species particles, temporary formation of unstable mixed structure, and stable creation of a Janus particle.

the initial simultaneous cooling, the Si temperature rises higher than that of Ag, due to heat induced by its subsequent faster growth rate (region III, Figure 6). Several spikes in the Si temperature correspond to events where two small primary Si nanoparticles collide and coalesce, forming increasingly larger nanoparticles, which contain almost all the Si atoms. Similar spikes are less pronounced and rarer in Ag, which clusters at a slower rate than Si. This is because the boiling point of Ag is much lower than that of Si, and hence the condensation into stable clusters requires a longer cooling time for the Ag atoms.

Having aggregated into monoelemental clusters, the two cluster types ultimately collided or coalesced to form hybrid particles, later in the process. While collisions occurred, analysis of the MD simulations demonstrated that only certain cases resulted in stable conjoined structures, while in many other cases the dissimilar clusters rapidly decoupled to isolated single-species clusters again. An example of a collision event between primary particles of different species which did not result in a stable hybrid nanoparticle is indicated by region IV in Figure 6, occurring at around 78 ns. The two species exchange energies violently, with the temperature of Si dropping by around 500 K and that of Ag rising by around 300 K. A snapshot of this event (which corresponds to 1:17" of the animation movie in the Supporting Information) is depicted in Figure 5d. The two clusters partially coalesce (a small spike is observed in the graph showing the number of mixed species neighboring atoms, not shown here) but do not stay together. Numerous similar events have been observed in MD simulations over a range of simulation conditions.

In contrast, later on, after around 110 ns (1:42–1:47" of animation Movie S1) another collision occurs between the Si and the Ag nanoparticles (indicated by region V, Figure 6), this time leading to a stable Si–Ag hybrid nanoparticle (Figure 5e). This configuration was stable, unlike the previous one, because at this stage both clusters shared the same temperature before the collision. In the previous case, the Si cluster was about 1000 K hotter than the Ag, preventing the atoms from staying together for long. Similar cases were observed in various simulation runs, with the two clusters sticking together for longer periods when their precollision temperature difference was less pronounced, ultimately reaching a limit wherein the

thermal difference was small enough to allow stable hybrid clusters to form. Note that practical limitations regarding the simulation time and system size meant that the number of chance collision events we could observe was limited; therefore, core–satellite structures were not explicitly created in the simulations, since they require multiple collision events. We did, however, observe collisions of relatively small Ag nanoparticles with larger Si ones, with further small Ag particles in proximity (Figure S6), which is the basic recipe for core–satellite structure formation.

The presented results show that, for the current deposition configuration, hybrid clusters of amorphous Si and crystalline Ag, with various sizes and microstructures, were produced. Previous work on the Si–Ag system, by the authors and others, reported a range of complex interactions resulting from the unique phase diagram of Si–Ag alloys, including metal-induced crystallization, liquid–liquid phase transitions, eutectic alloy formation, metastable silicide formation, solid phase segregation, and recalescence.^{22,23,33} Our molecular dynamics simulations clearly demonstrate that the two species nucleate separately during the early stages of growth, while colliding to form stable hybrid structures once sufficient cooling had taken place. Our proposed model is that the quantity and size distributions of the respective Si and Ag particles, once this stable hybrid collision phase begins, then governs the final microstructure, and specifically whether the Janus or core–satellite structure is formed. Considering the Si particles as hosts upon which the Ag particles reside, the Janus structure results from stable collisions with relatively fewer, but larger, Ag particles, while the core–satellite structures result from collisions with relatively more, but smaller, Ag particles. One may consider that in the absence of Si particles the Ag particles would continue to ripen by further collisions, reducing in quantity but increasing in size; but the presence of the Si carrier particles leads to a freeze frame of the Ag cluster number density and size distribution at the time of transition to stable hybrid structures. To address the trend from collisions of numerous small Ag clusters (core–satellite) to few large Ag clusters (Janus) as a function of increased magnetron power, we must consider the effect of magnetron power on the nucleation and growth of the Ag clusters, prior to their stable collision with Si particles. While the processes in the aggregation zone are numerous and complex, the increased magnetron discharge power and associated temperature will result in a reduced rate constant K for three-body collisions (nucleation dimer formation)⁴⁸ and an increased rate constant k_0 for atomic attachment to an existing cluster (growth).¹⁴ In relative terms, this is consistent with the observation that relatively fewer, but larger Ag particles collide with Si host particles at higher magnetron power, and vice versa.

Experimentally, the fact that all Si domains in the final ensembles are amorphous provides compelling evidence that the complex chemical intermixing reported previously (which ultimately leads to Si crystallization)³³ is not a significant factor here, which is reasonable given the very different synthesis configuration. Rather, the MD simulations show parallel pre-growth of independent same-species clusters and little postcollision chemical interaction, which is consistent with the experimentally observed binary nanoparticles.

CONCLUSIONS

In conclusion, Ag and Si were cosputtered from two independent neighboring targets to enable heterogeneous gas-

phase nanoparticle condensation. First, the possibility to extend the hybrid ensemble size from 5 up to 15 nm, by appropriate tuning of the deposition parameters in tandem with live feedback from the *in situ* mass filter, was demonstrated. Subsequently, characterization showed that the hybrid nanoparticles consisted of well-defined domains of elemental Ag (crystalline) and Si (amorphous), with no detectable intermixing. The size and quantity of the constituent Ag domains was manipulated by varying the Ag magnetron sputtering power, resulting in Janus and core–satellite structures. MD simulations show that Si and Ag nanoclusters nucleate separately from the corresponding supersaturated vapors, then grow and coalesce into larger nanoparticles, and form stable conjoined ensembles once the temperatures have reduced sufficiently to allow the formation of a stable structure. The present study represents significant progress toward achieving controlled synthesis of bespoke metal/semiconductor nanoparticles with different elemental compositions and structures. It increases our understanding of the growth kinetics and provides a powerful platform to test theoretical forecasts of immiscible metal/semiconductor systems.

ASSOCIATED CONTENT

Supporting Information

Animation movie of MD simulation run (Movie S1); Caption for Animation Movie S1; EDX spectra acquired from the indicated regions of core-satellite and Janus Si-Ag nanoparticles (Figure S1); Bright-field HRTEM image with corresponding FFTs for core-satellite and Janus nanostructure Si-Ag nanoparticles (Figure S2); HAADF-STEM image and EDX spectra of pure-Si nanoparticles (Figure S3); HAADF-STEM image and EDX spectra of pure-Ag nanoparticles (Figure S4); Bright-field TEM and HAADF-STEM images of sequentially deposited Si and Ag nanoparticles (Figure S5); Snapshot of MD simulation run containing 1000 Ar, 800 Si, and 200 Ag atoms (Figure S6). This material is available free of charge via the Internet at <http://pubs.acs.org>.

AUTHOR INFORMATION

Corresponding Authors

*Tel: +81-10-62334204; e-mail c.cassidy@oist.jp (C.C.).

*Tel: +81-(0)98-966-8622; e-mail: mukhles@oist.jp (M.S.).

Notes

The authors declare no competing financial interest.

ACKNOWLEDGMENTS

We thank Dr. Kouji Inoke from FEI Company (Tokyo, Japan) for assistance in STEM imaging. We are also grateful to the Finnish IT Centre for Science CSC and the Finnish Grid Infrastructure (FGI) for grants of computer time.

REFERENCES

- (1) Lattuada, M.; Hatton, T. A. Synthesis, Properties and Applications of Janus Nanoparticles. *Nano Today* **2011**, *6*, 286–308.
- (2) Ferrando, R.; Jellinek, J.; Johnston, R. L. Nanoalloys: From Theory to Applications of Alloy Clusters and Nanoparticles. *Chem. Rev.* **2008**, *108*, 846–872.
- (3) Hu, J.; Zhou, S.; Sun, Y.; Fang, X.; Wu, L. Fabrication, Properties and Applications of Janus Particles. *Chem. Soc. Rev.* **2012**, *41*, 4356–4378.
- (4) You, H.; Yang, S.; Dinga, B.; Yang, H. Synthesis of Colloidal Metal and Metal Alloy Nanoparticles for Electrochemical Energy Applications. *Chem. Soc. Rev.* **2013**, *42*, 2880–2904.

- (5) Peng, Z.; Yang, H. Synthesis and Oxygen Reduction Electrocatalytic Property of Pt-on-Pd Bimetallic Heteronanostructures. *J. Am. Chem. Soc.* **2009**, *131*, 7542–7543.
- (6) Fan, J.; Chu, P. K. Group IV Nanoparticles: Synthesis, Properties, and Biological Applications. *Small* **2010**, *6*, 2080–2098.
- (7) Wang, X.; Zhuang, J.; Peng, Q.; Li, Y. A General Strategy for Nanocrystal Synthesis. *Nature* **2005**, *437*, 121–124.
- (8) Alayoglu, S.; Eichhorn, B. Rh–Pt Bimetallic Catalysts: Synthesis, Characterization, and Catalysis of Core–Shell, Alloy, and Monometallic Nanoparticles. *J. Am. Chem. Soc.* **2008**, *130*, 17479–17486.
- (9) Wang, H.; Chen, L.; Feng, Y.; Chen, H. Exploiting Core–Shell Synergy for Nanosynthesis and Mechanistic Investigation. *Acc. Chem. Res.* **2013**, *46*, 1636–1646.
- (10) Ferrer, D.; Torres-Castro, A.; Gao, X.; Sepulveda-Guzman, S.; Ortiz-Mendez, U.; Jose-Yacaman, M. Three-Layer Core/Shell Structure in Au–Pd Bimetallic Nanoparticles. *Nano Lett.* **2007**, *7*, 1701–1705.
- (11) Yang, Q.; de Vries, M. H.; Picchioni, F.; Loos, K. A Novel Method of Preparing Metallic Janus Silica Particles Using Supercritical Carbon Dioxide. *Nanoscale* **2013**, *5*, 10420–10427.
- (12) Mark, A. G.; Gibbs, J. G.; Lee, T.-C.; Fischer, P. Hybrid Nanocolloids with Programmed Three-Dimensional Shape and Material Composition. *Nat. Mater.* **2013**, *12*, 802–807.
- (13) Langlois, C.; Li, Z. L.; Yuan, J.; Alloyeau, D.; Nelayah, J.; Bochicchio, D.; Ferrandod, R.; Ricolleau, C. Transition from Core–Shell to Janus Chemical Configuration for Bimetallic Nanoparticles. *Nanoscale* **2012**, *4*, 3381–3388.
- (14) Kashtanov, P. V.; Smirnov, B. M.; Hippler, R. Magnetron Plasma and Nanotechnology. *Phys.-Usp.* **2007**, *50*, 455–488.
- (15) Haberland, H.; Mall, M.; Moseler, M.; Qiang, Y.; Reiners, T.; Thurner, Y. Filling of Micron-Sized Contact Holes with Copper by Energetic Cluster Impact. *J. Vac. Sci. Technol., A* **1994**, *12*, 2925–2930.
- (16) Bromann, K.; Felix, C.; Brune, H.; Harbich, W.; Monot, R.; Buttet, J.; Kern, K. Controlled Deposition of Size-Selected Silver Nanoclusters. *Science* **1996**, *274*, 956–958.
- (17) Palmer, R. E.; Pratontep, S.; Boyen, H.-G. Nanostructured Surfaces from Size-Selected Clusters. *Nat. Mater.* **2003**, *2*, 443–448.
- (18) Couillard, M.; Pratontep, S.; Palmer, R. E. Metastable, Ordered Arrays of Size-Selected Ag Clusters on Graphite. *Appl. Phys. Lett.* **2006**, *82*, 2595–2597.
- (19) Shyjumon, I.; Gopinadhan, M.; Helm, C. A.; Smirnov, B. M.; Hippler, R. Deposition of Titanium/Titanium Oxide Clusters Produced by Magnetron Sputtering. *Thin Solid Films* **2006**, *500*, 41–51.
- (20) Xu, Y. H.; Wang, J. P. Direct Gas-Phase Synthesis of Heterostructured Nanoparticles through Phase Separation and Surface Segregation. *Adv. Mater.* **2008**, *20*, 994–999.
- (21) Yin, F.; Wang, Z. W.; Palmer, R. E. Controlled Formation of Mass-Selected Cu–Au Core–Shell Cluster Beams. *J. Am. Chem. Soc.* **2011**, *133*, 10325–10327.
- (22) Olesinski, R. W.; Gokhale, A. B.; Abbaschian, G. J. The Ag–Si (Silver–Silicon) System. *Bull. Alloy Phase Diagrams* **1989**, *10*, 635–640.
- (23) Bokhonov, B.; Korchagin, M. In-Situ Investigation of the Formation of Eutectic Alloys in the Systems Silicon–Silver and Silicon–Copper. *J. Alloys Compd.* **2002**, *335*, 149–156.
- (24) Chen, K.-H.; Pu, Y.-C.; Chang, K.-D.; Liang, Y.-F.; Liu, C.-M.; Yeh, J.-W.; Shih, H.-C.; Hsu, Y.-J. Ag-Nanoparticle-Decorated SiO₂ Nanospheres Exhibiting Remarkable Plasmon-Mediated Photocatalytic Properties. *J. Phys. Chem. C* **2012**, *116*, 19039–19045.
- (25) Chen, T. H.; Jean, R.-D.; Chiu, K.-C.; Chen, C.-H.; Liu, D.-M. Transparent SiO₂-Ag Core–Satellite Nanoparticle Assembled Layer for Plasmonic-Based Chemical Sensors. *Appl. Phys. Lett.* **2012**, *100*, 223101.
- (26) Ferry, V. E.; Sweatlock, L. A.; Pacifici, D.; Atwater, H. A. Plasmonic Nanostructure Design for Efficient Light Coupling into Solar Cells. *Nano Lett.* **2008**, *8*, 4391–4397.
- (27) Allen, M. P.; Tildesley, D. J. *Computer Simulation of Liquids*; Oxford University Press: Oxford, England, 1989.
- (28) Kesälä, E.; Kuronen, A.; Nordlund, K. Molecular Dynamics Simulation of Pressure Dependence of Cluster Growth in Inert Gas Condensation. *Phys. Rev. B* **2007**, *75*, 174121.
- (29) Harjunmaa, A.; Nordlund, K. Molecular Dynamics Simulations of Si/Ge Cluster Condensation. *Comput. Mater. Sci.* **2009**, *47*, 456–459.
- (30) Krashnachtchekov, P.; Albe, K.; Averback, R. S. Simulations of the Inert Gas Condensation Processes. *Int. J. Mater. Res.* **2003**, *94*, 1098–1105.
- (31) Lümmen, N.; Kraska, T. Molecular Dynamics Investigation of Homogeneous Nucleation and Cluster Growth of Platinum Clusters from Supersaturated Vapor. *Nanotechnology* **2005**, *16*, 2870–2877.
- (32) Muller, M.; Albe, K. Concentration of Thermal Vacancies in Metallic Nanoparticles. *Acta Mater.* **2007**, *55*, 3237–3244.
- (33) Cassidy, C.; Singh, V.; Grammatikopoulos, P.; Djurabekova, F.; Nordlund, K.; Sowwan, M. Incubation of Silicon Nanoparticles with Silver Atoms. *Sci. Rep.* **2013**, *3*, 3083.
- (34) Foiles, S. M.; Baskes, M. I.; Daw, M. S. Embedded-Atom-Method Functions for the FCC Metals Cu, Ag, Au, Ni, Pd, Pt, and Their Alloys. *Phys. Rev. B* **1986**, *33*, 7983–7991; Erratum: *Phys. Rev. B* **1988**, *37*, 10378.
- (35) Stillinger, F. H.; Weber, T. A. Computer Simulation of Local Order in Condensed Phases of Silicon. *Phys. Rev. B* **1985**, *31*, 5262–5271.
- (36) Nordlund, K.; Runeberg, N.; Sundholm, D. Repulsive Interatomic Potentials Calculated Using Hartree-Fock and Density-Functional Theory Methods. *Nucl. Instrum. Methods Phys. Res., Sect. B* **1997**, *132*, 45–54.
- (37) Tersoff, J. New Empirical Approach for the Structure and Energy of Covalent Systems. *Phys. Rev. B* **1988**, *37*, 6991–7000.
- (38) Ziegler, J. F.; Biersack, J. P.; Littmark, U. *The Stopping and Range of Ions in Matter*; Pergamon: New York, 1985.
- (39) Kittel, C. *Introduction to Solid State Physics*, 6th ed.; Wiley: New York, 1986.
- (40) Berendsen, H. J. C.; Postma, J. P. M.; van Gunsteren, W. F.; DiNola, A.; Haak, J. R. Molecular Dynamics with Coupling to an External Bath. *J. Chem. Phys.* **1984**, *81*, 3684–3690.
- (41) Cassidy, C.; Singh, V.; Hawash, Z.; Bohra, M.; Kim, J. H.; Sowwan, M. Size-Controlled Deposition of Ag and Si Nanoparticle Structures with Gas-Aggregated Sputtering. *MRS Proc.* **2013**, *1546*, 106.
- (42) Haberland, H.; Karrais, M.; Mall, M.; Thurner, Y. Thin Films from Energetic Cluster Impact: A Feasibility Study. *J. Vac. Sci. Technol., A* **1992**, *10*, 3266–3271.
- (43) Nielsen, R. M.; Murphy, S.; Strebel, C.; Johansson, M.; Chorkendorff, I.; Nielsen, J. H. The Morphology of Mass Selected Ruthenium Nanoparticles from a Magnetron-Sputter Gas-Aggregation Source. *J. Nanopart. Res.* **2010**, *12*, 1249–1262.
- (44) Pack, R. T.; Walker, R. B.; Kendrick, B. K. Three-Body Collision Contributions to Recombination and Collision-Induced Dissociation. I. Cross sections. *J. Chem. Phys.* **1998**, *109*, 6701–6713.
- (45) Pack, R. T.; Walker, R. B.; Kendrick, B. K. Three-Body Collision Contributions to Recombination and Collision-Induced Dissociation. II. Kinetics. *J. Chem. Phys.* **1998**, *109*, 6714–6724.
- (46) Westergren, J.; Grönbeck, H.; Rosen, A.; Nordholm, S. Statistical Theory of Cluster Cooling in Rare Gas. I. Energy Transfer Analysis for Palladium Clusters in Helium. *J. Chem. Phys.* **1998**, *109*, 9848.
- (47) Stukowski, A. Visualization and Analysis of Atomistic Simulation Data with OVITO—the Open Visualization Tool. *Modeling Simul. Mater. Sci. Eng.* **2010**, *18*, 015012.
- (48) Smirnov, V. M. Processes in Expanding and Condensing Gases. *Phys.-Usp.* **1994**, *37*, 621–658.